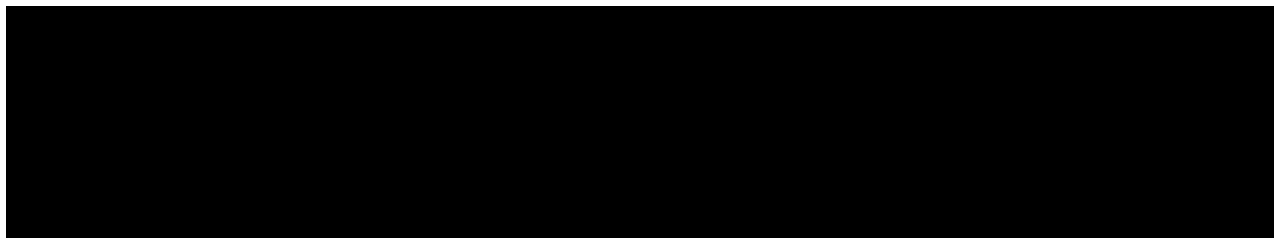


Three parallel orange diagonal lines are located in the top left corner of the page.

# **Marine Aquaculture Site **Loch Hourn****

## **Appendix 5. Hydrodynamic Model Description**

**Mowi Scotland Limited**  
**December 2021**

A solid black rectangular box is positioned at the bottom of the page, spanning most of its width.

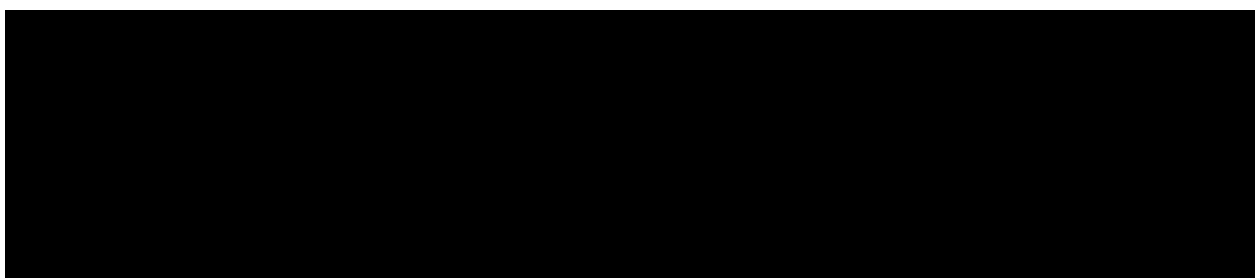


# Hydrodynamic Model Description

## CREAG AN SAGAIRT, LOCH HOURN

CAR/L/1105276

September 2021



**CONTENTS**

	Page
<b>1. MODEL DESCRIPTION</b>	<b>4</b>
<b>2. CONFIGURATION AND BOUNDARY FORCING FOR LOCH HOURN</b>	<b>5</b>
<b>3. MODEL CALIBRATION AND VALIDATION</b>	<b>8</b>
<b>3.1 Calibration, September – November 2018, ID246</b>	<b>9</b>
<b>3.2 Validation: November 2018 – February 2019, ID253</b>	<b>12</b>
<b>3.3 Validation: November 2018 – February 2019, ID254</b>	<b>15</b>
<b>3.4 Validation: April – July 2019, ID275</b>	<b>17</b>
<b>4. MODELLED FLOW FIELDS</b>	<b>20</b>
<b>5. REFERENCES</b>	<b>21</b>

## LIST OF FIGURES

- Figure 1. The mesh and domain of the East Coast of Lewis and Harris (ECLH) sub-model of the Scottish Shelf Model (Marine Scotland, 2016). 6
- Figure 2. The unstructured mesh around the Loch Hourn site in the modified model grid, with the proposed cage locations indicated (•). 6
- Figure 3. Model water depths (m) in the area around Loch Hourn salmon farm. 7
- Figure 4. Profiles of water temperature (°C), salinity (PSU) and density (kg m<sup>-3</sup>) from Loch Hourn, taken on 1<sup>st</sup> April 2021. Profiles from Stations 7 (during ebb tide) and 12 (during flood tide) are shown, together with a chart of the locations of all 15 stations sampled. 8
- Figure 5. Locations of the ADCP deployments relative to the 8 pens at the Loch Hourn site. 9
- Figure 6. Comparison between observed and modelled sea surface height from September – November 2018 (ADCP deployment ID246) using model parameter values from Table 1. Both the full record (left) and a subset of 15 days (right) are shown. Observed data are in blue, model results in red. 10
- Figure 7. Comparison between observed and modelled East (top) and North (bottom) components of velocity at the ADCP location for 15 days in September – November 2018 (ID246). Observed data are in blue, model results in red. 11
- Figure 8. Scatter plot of observed and modelled velocity at the ADCP location from September – November 2018 (ID246). Observed data are in blue, model results in red. 11
- Figure 9. Histograms of observed and modelled speed (top) and direction (bottom) at the ADCP location from September – November 2018 (ID246). Observed data are in blue, model results in red. 12
- Figure 10. Comparison between observed and modelled sea surface height from November 2018 – February 2019 (ADCP deployment ID253) using model parameter values from Table 1. Both the full record (left) and a subset of 15 days (right) are shown. Observed data are in blue, model results in red. 13
- Figure 11. Comparison between observed and modelled East (top) and North (bottom) components of velocity at the ADCP location for 15 days in November 2018 – February 2019 (ID253). Observed data are in blue, model results in red. 13
- Figure 12. Scatter plot of observed and modelled velocity at the ADCP location from November 2018 – February 2019 (ID253). Observed data are in blue, model results in red. 14

- Figure 13. Histograms of observed and modelled current speed (top) and direction (bottom) at the ADCP location from November 2018 – February 2019 (ID253). Observed data are in blue, model results in red. 14
- Figure 14. Comparison between observed and modelled sea surface height from November 2018 – February 2019 (ADCP deployment ID254) using model parameter values from Table 1. Both the full record (left) and a subset of 15 days (right) are shown. Observed data are in blue, model results in red. 15
- Figure 15. Comparison between observed and modelled East (top) and North (bottom) components of velocity at the ADCP location for 15 days in November 2018 – February 2019 (ID254). Observed data are in blue, model results in red. 16
- Figure 16. Scatter plot of observed and modelled velocity at the ADCP location from November 2018 – February 2019 (ID254). Observed data are in blue, model results in red. 16
- Figure 17. Histograms of observed and modelled current speed (top) and direction (bottom) at the ADCP location from November 2018 – February 2019 (ID254). Observed data are in blue, model results in red. 17
- Figure 18. Comparison between observed and modelled sea surface height from April – July 2019 (ID275) using model parameter values from Table 1. Both the full record (left) and a subset of 15 days (right) are shown. Observed data are in blue, model results in red. 18
- Figure 19. Comparison between observed and modelled East (top) and North (bottom) components of velocity at the ADCP location for 15 days in April – July 2019 (ID275). Observed data are in blue, model results in red. 18
- Figure 20. Scatter plot of observed and modelled velocity at the ADCP location from April – July 2019 (ID275). Observed data are in blue, model results in red. 19
- Figure 21. Histograms of observed and modelled speed (top) and direction (bottom) at the ADCP location from April – July 2019 (ID275). Observed data are in blue, model results in red. 19
- Figure 22. Modelled flood (top) and ebb (bottom) surface current vectors during spring tides on 25<sup>th</sup> April 2020 and 22<sup>nd</sup> April 2020 respectively. For clarity, only 25% of the model vectors are shown, and vectors with a speed greater than 0.3 m s<sup>-1</sup> are also not shown. 20
- Figure 23. Mean modelled current vectors from 30<sup>th</sup> April – 4<sup>th</sup> July 2020 (ID275). For clarity, only 25% of the model vectors are shown, and vectors with a mean speed greater than 0.2 m s<sup>-1</sup> are also not shown 21

## LIST OF TABLES

Table 1. Parameter values chosen for the RiCOM model during the calibration simulations. .	9
Table 2. Model performance statistics for sea surface height (SSH) and East and North velocity at the ADCP location from August – October 2016 (ID113).....	10
Table 3. Model performance statistics for sea surface height (SSH), and East and North velocity at the ADCP location from the calibration simulation, November 2018 – February 2019 (ID253).....	12
Table 4. Model performance statistics for sea surface height (SSH), and East and North velocity at the ADCP location from the calibration simulation, November 2018 – February 2019 (ID253).....	15
Table 5. Model performance statistics for sea surface height (SSH), and East and North velocity at the ADCP location from the calibration simulation, April – July 2019 (ID275). .....	17

## 1. Model Description

The hydrodynamic model used in this study was RiCOM (River and Coastal Ocean Model), a general-purpose hydrodynamics and transport model, which solves the standard Reynolds-averaged Navier-Stokes equation (RANS) and the incompressibility condition, applying the hydrostatic and Boussinesq approximations. It has been tested on a variety of benchmarks against both analytical and experimental data sets (e.g. Walters & Casulli 1998; Walters 2005a, b). The model has been previously used to investigate the inundation risk from tsunamis and storm surge on the New Zealand coastline (Walters 2005a; Gillibrand et al. 2011; Lane et al. 2011), to study tidal currents in high energy tidal environments (Walters et al. 2010) and, more recently, to study tidal energy resource (Plew & Stevens 2013; Walters et al. 2013; Walters 2016) and the effects of energy extraction on the ambient environment (McIlvenny et al. 2016; Gillibrand et al. 2016).

The basic equations considered here are the three-dimensional (3D) shallow water equations, derived from the Reynolds-averaged Navier-Stokes equations by using the hydrostatic assumption and the Boussinesq approximation. The continuity equation for incompressible flows is:

$$\nabla \cdot \mathbf{u} + \frac{\partial w}{\partial z} = 0 \quad (1)$$

where  $\mathbf{u}(x,y,z,t)$  is the horizontal velocity vector,  $w(x,y,z,t)$  is the vertical velocity,  $\nabla$  is the horizontal gradient operator, and  $z$  is the vertical coordinate. The momentum equation in non-conservative form is given by:

$$\frac{D\mathbf{u}}{Dt} + f\hat{z} \times \mathbf{u} + \frac{1}{\rho_0} \nabla p - \frac{\partial}{\partial z} \left( A_V \frac{\partial \mathbf{u}}{\partial z} \right) - \nabla \cdot (A_h \nabla \mathbf{u}) + \mathbf{F} = 0 \quad (2)$$

where  $t$  is time;  $f(x,y)$  is the Coriolis parameter;  $\hat{z}$  is the upward unit vector;  $p(x,y,z,t)$  is pressure;  $\rho_0$  is a reference density;  $A_V(x,y,z,t)$  and  $A_h(x,y,z,t)$  are the vertical and horizontal eddy viscosities respectively;  $\mathbf{F}$  represents body forces including form drag from obstacles in the flow; and  $x, y$  are the horizontal coordinates aligned to the east and north respectively.

The free surface equation is formed by vertically integrating the continuity equation and applying the kinematic free surface and bottom boundary conditions:

$$\frac{\partial \eta}{\partial t} - \nabla \cdot \left( \int_{-H}^{\eta} \mathbf{u} dz \right) = 0 \quad (3)$$

where  $H$  is the water depth relative to the mean level of the sea.

The model can be run in two- or three-dimensional mode. Frictional stress,  $\tau_b$ , is applied at the seabed as a quadratic function of velocity:

$$\tau_b = \rho C_D U_b |U_b| \quad (4)$$

where  $\rho = 1025 \text{ kg m}^{-3}$  is the water density. The velocity,  $U_b$ , is either the velocity at the lowest sigma layer if the model is run in 3D or the depth-averaged velocity if run in 2D. The drag coefficient,  $C_D$ , can be either a constant or calculated from the bed roughness lengthscale,  $z_0$ , using:

$$C_D = \left( \frac{\kappa}{\ln((z_b + z_0)/z_0)} \right)^2 \quad (5)$$

where  $\kappa=0.4$  is von Karman's constant, and  $z_b$  is the height above the bed of the lowest velocity point.

Wind forcing was applied as a surface stress calculated from hourly wind speed and direction. Wind stress was calculated from the wind velocity by a standard quadratic relation:

$$\tau_x = \rho_a C_S u W \quad (6a)$$

$$\tau_y = \rho_a C_S v W \quad (6b)$$

where  $(u,v)$  are the East and North components of wind velocity respectively,  $W$  is the wind speed ( $W = [u^2+v^2]^{1/2}$ ),  $\rho_a$  is the density of air, and the surface drag coefficient  $C_S$  is calculated following Wu (1982) or Large and Pond (1981).

The equations are discretized on an unstructured grid of triangular elements which permits greater resolution of complex coastlines. The momentum and free surface equations are solved using semi-implicit techniques to optimize solution time and avoid the CFL stability constraint (Walters 2016). The material derivative in (2) is discretized using semi-Lagrangian methods to remove stability constraints on advection (Casulli, 1987; Walters et al. 2008). The Coriolis term is solved using a 3<sup>rd</sup> order Adams-Bashforth method (Walters et al. 2009). Full details of the model discretization and solution methods can be found in Walters et al. (2013) and Walters (2016). The solution methods provide a fast, accurate and robust code that runs efficiently on multi-core desktop workstations with shared memory using OpenMP. Full details of the model discretization and solution methods, including the basis of the application to tidal energy, are given by Walters et al. (2013) and Walters (2016).

## 2. Configuration and Boundary Forcing for Loch Hourn

The unstructured mesh used in the model was adapted from East Coast of Lewis and Harris (ECLH) sub-model mesh (Figure 1) of the Scottish Shelf Model (SSM; MS, 2016). Model resolution was enhanced in the Loch Hourn and Sound of Sleat region particularly around the Mowi site (Figure 2). The spatial resolution of the model varied from 25m in some inshore waters to 5 km along the open boundary. In total, the model consisted of 42,286 nodes and 79,245 triangular elements.

Bathymetry in the original ECLH model is poor in the Loch Hourn area. Instead, we took bathymetry from the UK Hydrographic Office portal (<https://www.admiralty.co.uk/digital-services/data-solutions/admiralty-marine-data-portal>) and interpolated these data onto the node locations in Loch Hourn and the Sound of Sleat region (Figure 3).

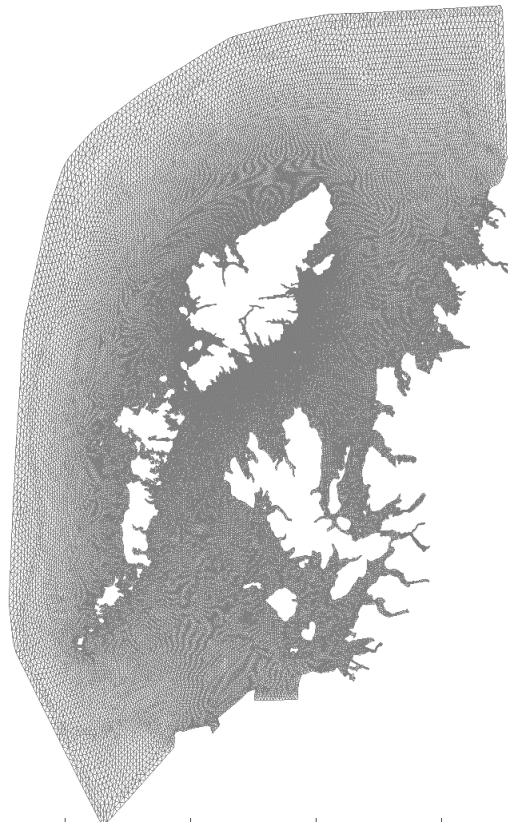


Figure 1. The mesh and domain of the East Coast of Lewis and Harris (ECLH) sub-model of the Scottish Shelf Model (Marine Scotland, 2016).

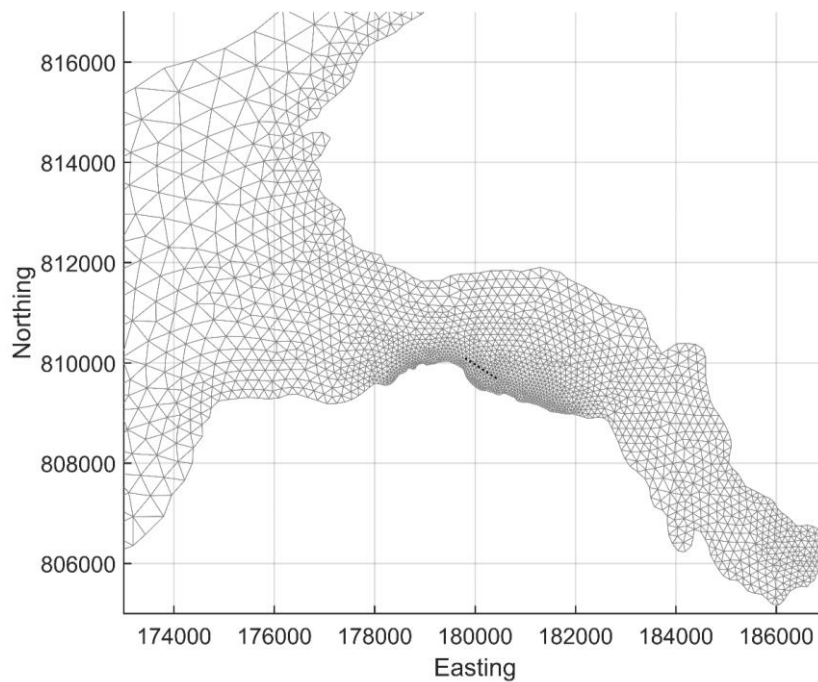


Figure 2. The unstructured mesh around the Loch Hourn site in the modified model grid, with the proposed cage locations indicated (•).

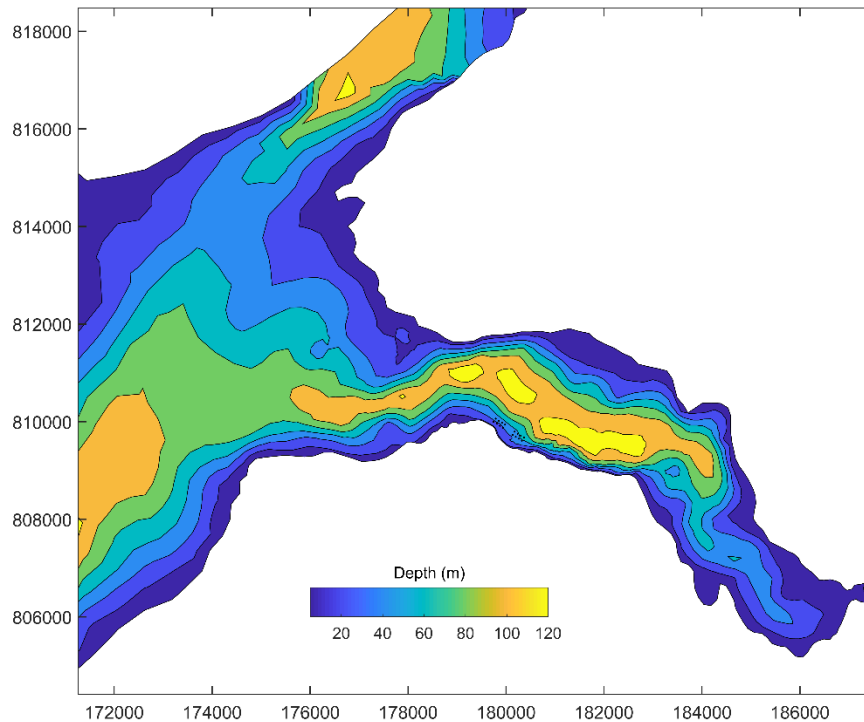


Figure 3. Model water depths (m) in the area around Loch Hourn salmon farm.

The model was forced along its open boundary by eight tidal constituents ( $O_1$ ,  $K_1$ ,  $Q_1$ ,  $P_1$ ,  $M_2$ ,  $S_2$ ,  $N_2$ ,  $K_2$ ), amplitudes and phase of which were obtained from the full Scottish Shelf Model. Spatially- and temporally-varying wind speed and direction data were taken from the ERA5 global reanalysis dataset for the required simulation periods (ECMWF, 2021), with the data converted to surface stress using Equation 6.

The model was run in 2D vertically-averaged mode. Loch Hourn has one of the lowest freshwater/tidal flow ratios of Scottish sea lochs, ranked 86 out of 109 with an estimated salinity reduction of 0.2 PSU (Edwards and Sharples, 1986). Measurements of temperature and salinity profiles, taken in April 2021, confirmed that stratification is weak in the area around the farm (Figure 4). The adjacent Sound of Sleat and Kyle Rhea are also well-mixed due to strong tidal currents. Preliminary model simulations demonstrated a good comparison between model and current observations using a 2D (depth-averaged) approach. Consequently, the flow fields developed and used with NewDepomod were 2D barotropic simulations, but were modified following Lewis et al. (2017) to reflect the reduction in velocity near the seabed (see the accompanying waste solids deposition modelling report).

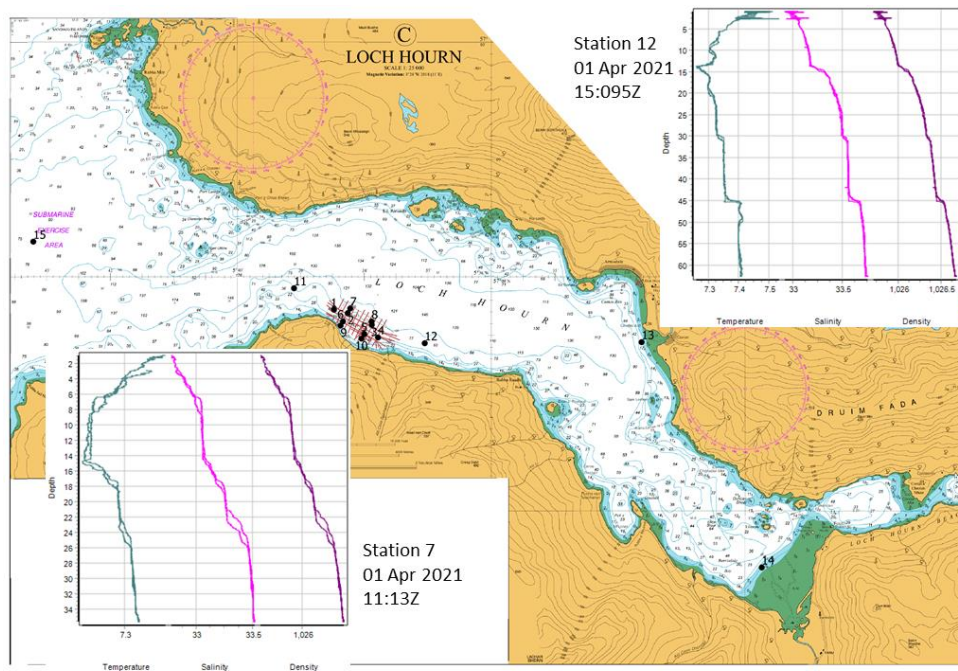


Figure 4. Profiles of water temperature ( $^{\circ}\text{C}$ ), salinity (PSU) and density ( $\text{kg m}^{-3}$ ) from Loch Hourn, taken on 1<sup>st</sup> April 2021. Profiles from Stations 7 (during ebb tide) and 12 (during flood tide) are shown, together with a chart of the locations of all 15 stations sampled.

### 3. Model Calibration and Validation

The RiCOM model has previously been calibrated against sea level and current meter data from the north of Scotland (Gillibrand et al. 2016). For the current study, the model was further calibrated against hydrographic data collected in the region of the farm site between 2018 – 2019. The data are described in the relevant hydrographic reports. In September 2018, an Acoustic Doppler Current Profiler (ADCPs) was deployed close to the farm site (Figure 5) until November 2018. Further deployments were made from November 2018 – February 2019 and April – July 2019. In all, 203 days of current data were used in this application. ADCP deployments provided both current velocity and seabed pressure data, which were used to calibrate and validate modelled velocity and sea surface height. The model was calibrated initially against data from September – November 2018, then validated against the data from the three remaining deployments.

For each simulation, the model was “spun-up” for three days with boundary forcing ramped up from zero over a period of 48 hours. The model state at the end of the 72-hour spin-up period was stored, and the main simulations “hot-started” from this state.

The following main simulations were performed, corresponding with the dates of the ADCP deployments:

- (i) Calibration: 11<sup>th</sup> September – 29<sup>th</sup> November 2018 (ID246)
- (ii) Validation: 29<sup>th</sup> November 2018 – 14<sup>th</sup> February 2019 (ID253 and ID254)
- (iii) Validation: 30<sup>th</sup> April – 4<sup>th</sup> July 2019 (ID275)

[Note that the dates above refer to the main simulations and that the spin-up simulations ran for three days prior to the start dates given above.]

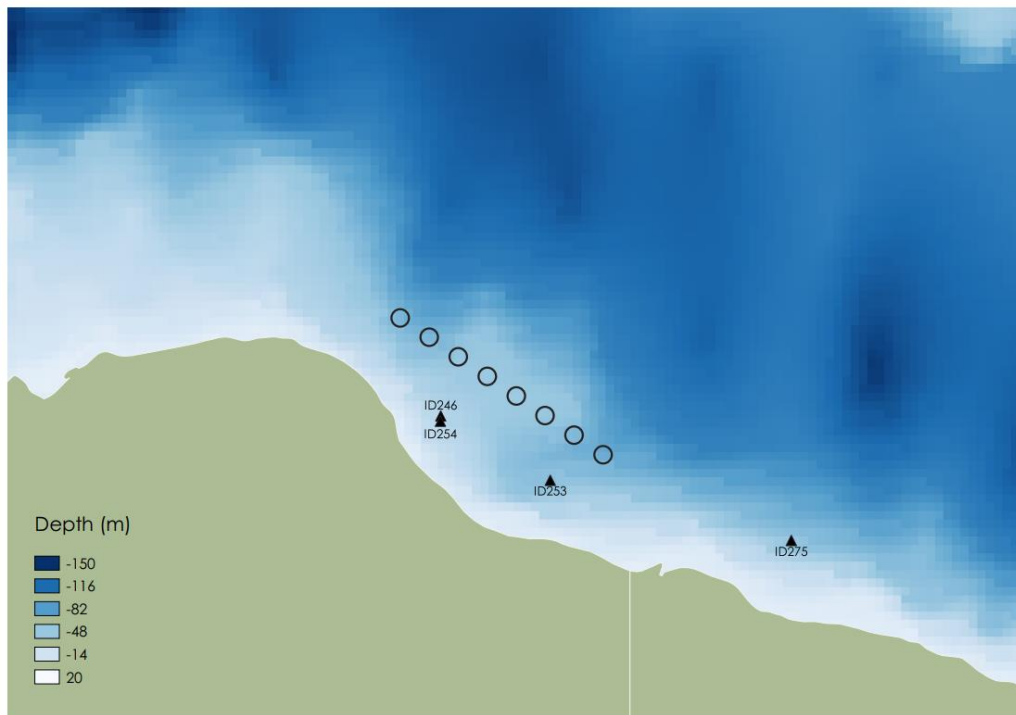


Figure 5. Locations of the ADCP deployments relative to the 8 pens at the Loch Hour site.

Model performance is assessed using three metrics: the mean absolute error (MAE), the root-mean-square error (RMSE) and the model skill ( $d_2$ ). The first two are standard measures of model accuracy; the third,  $d_2$ , is taken from Willmott et al. (1985) and lies in the range  $0 \leq d_2 \leq 1$ , with  $d_2 = 0$  implying zero model skill and  $d_2 = 1$  indicating perfect skill.

### 3.1 Calibration, September – November 2018, ID246

The calibration used observed depth and current velocity from the ADCP location to compare with modelled sea surface height (SSH) and velocity (ADCP deployment ID246). The model was calibrated by varying the value of the drag coefficient,  $C_D$ , in Equation A4, which determines the frictional effect of the seabed on the flow. Simulations were performed with a range of values of  $C_D$ , varying over the range  $0.002 \leq C_D \leq 0.02$ . After a number of simulations, a final parameter set was selected (Table 1).

Table 1. Parameter values chosen for the RiCOM model during the calibration simulations.

Parameter Description	Value
Drag coefficient, $C_D$	0.002
Number of vertical levels	1
Model time step (s)	72.0

The results of the calibration exercise are presented in Figure 6 – Figure 9 and Table 5. At the ADCP location, the sea surface height was reasonably accurately modelled, with model skill of 0.99. The mean absolute error (MAE) and root-mean-square error (RMSE) values of 0.18 m and 0.22 respectively are about 3.6% and 4.4% of the spring tide range respectively.

For the calibration period, the model skill scores were 0.72 and 0.62 for the East and North components of velocity respectively. RMSE values were 0.02 m s<sup>-1</sup> and 0.04 m s<sup>-1</sup> for the two components of velocity (Table 2). The scatter plots and histograms demonstrate that the modelled current had broadly the same magnitude and direction characteristics as the observed data (Figure 8 and Figure 9). The deployment ID246 was located close inshore, where bathymetry data is less certain and where measured currents are particularly sensitive to localised topographic steering.

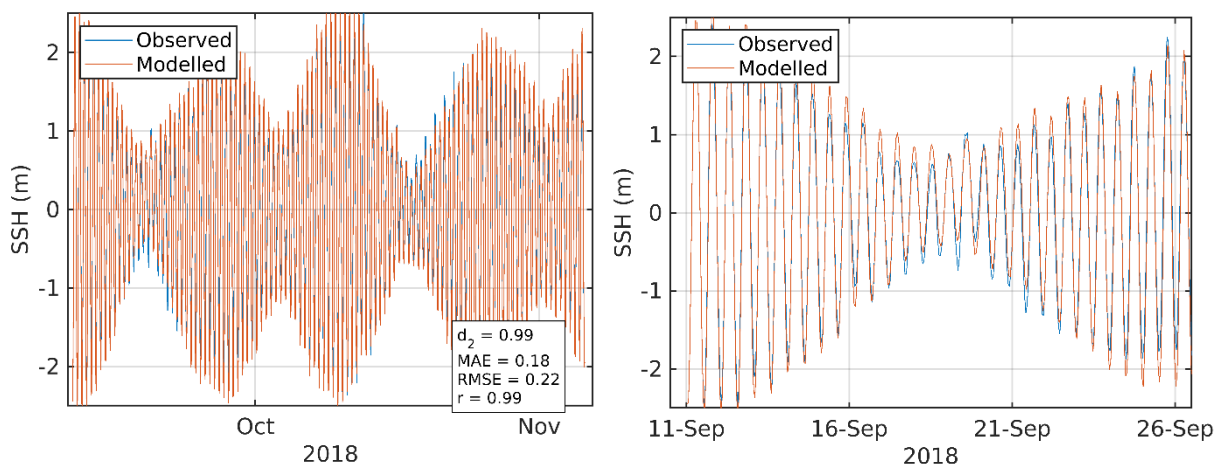


Figure 6. Comparison between observed and modelled sea surface height from September – November 2018 (ADCP deployment ID246) using model parameter values from Table 1 **Error! Reference source not found.** Both the full record (left) and a subset of 15 days (right) are shown. Observed data are in blue, model results in red.

Table 2. Model performance statistics for sea surface height (SSH) and East and North velocity at the ADCP location from August – October 2016 (ID113).

	SSH	East	North
Model skill, $d_2$	0.99	0.72	0.62
Mean Absolute Error (MAE)	0.18 m	0.02 m s <sup>-1</sup>	0.03 m s <sup>-1</sup>
Root-Mean-Square Error (RMSE)	0.22 m	0.02 m s <sup>-1</sup>	0.04 m s <sup>-1</sup>

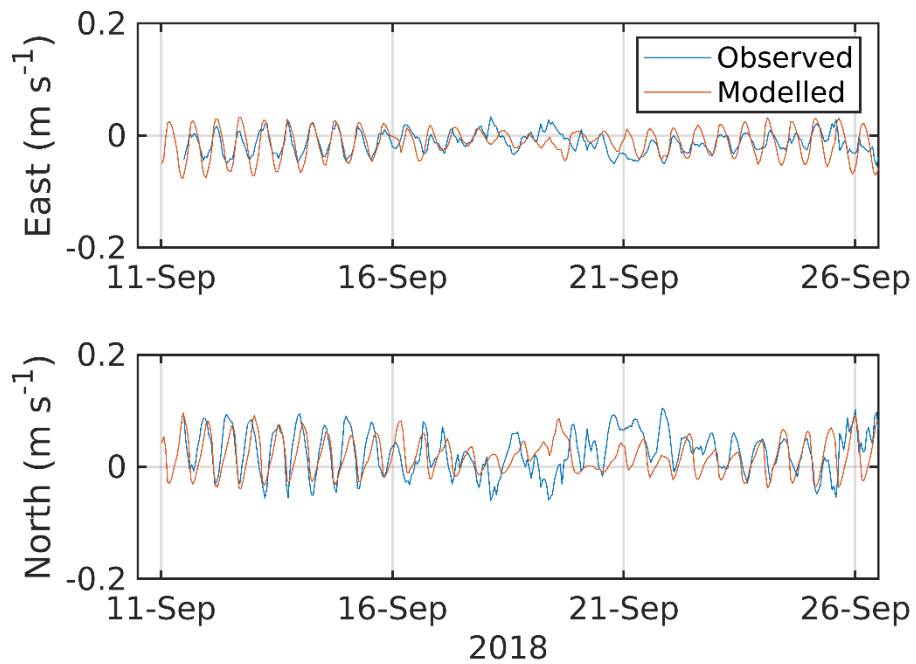


Figure 7. Comparison between observed and modelled East (top) and North (bottom) components of velocity at the ADCP location for 15 days in September – November 2018 (ID246). Observed data are in blue, model results in red.

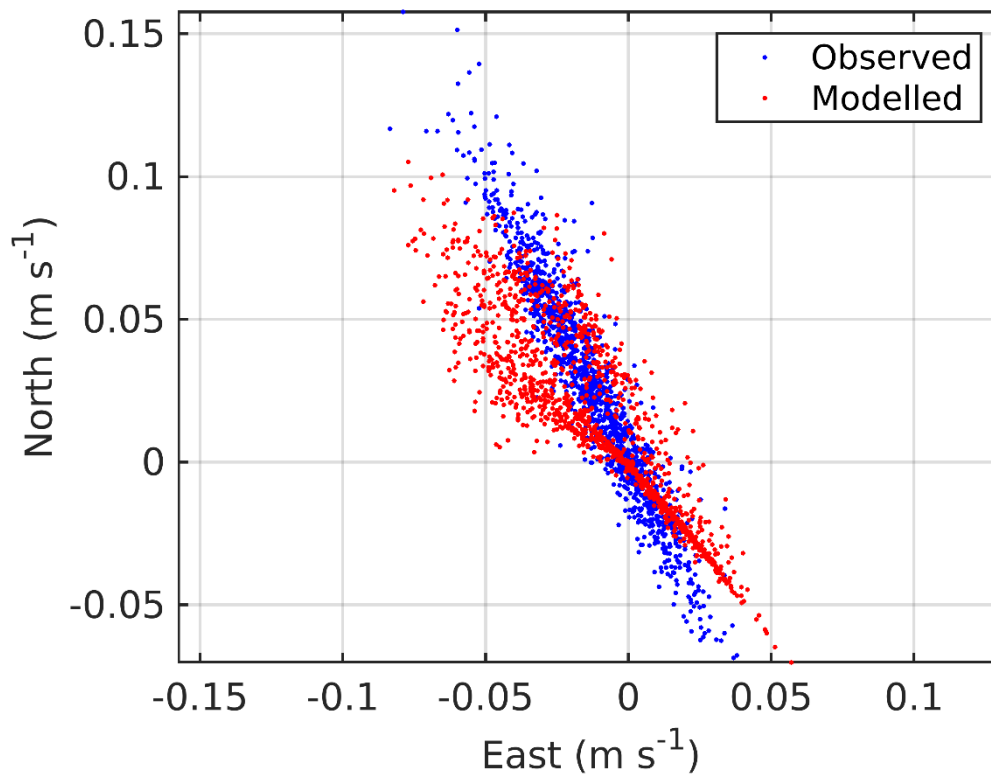


Figure 8. Scatter plot of observed and modelled velocity at the ADCP location from September – November 2018 (ID246). Observed data are in blue, model results in red.

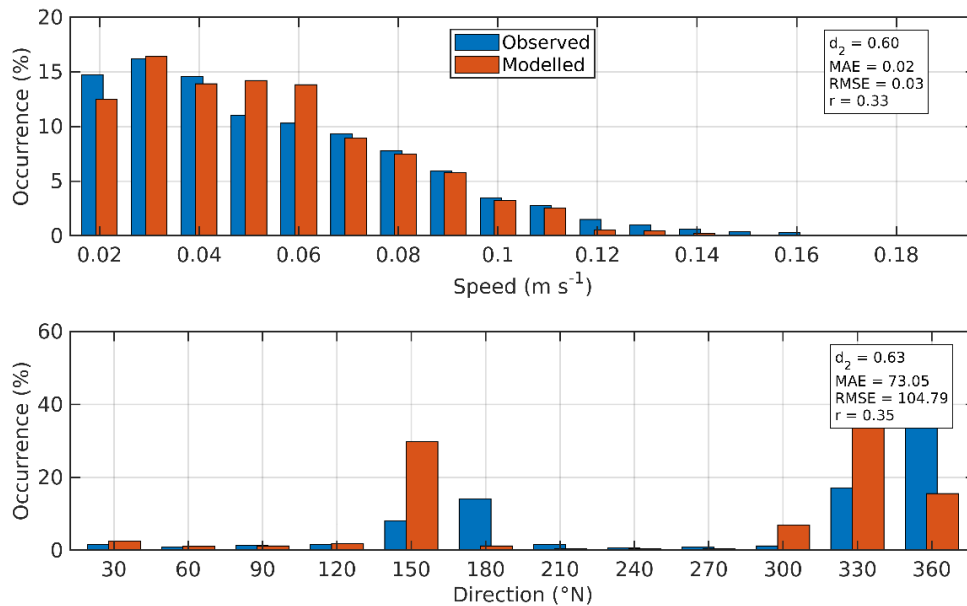


Figure 9. Histograms of observed and modelled speed (top) and direction (bottom) at the ADCP location from September – November 2018 (ID246). Observed data are in blue, model results in red.

### 3.2 Validation: November 2018 – February 2019, ID253

At the ADCP location, the sea surface height was reasonably accurately modelled, with model skill of 0.99 (Figure 10, Table 3). The mean absolute error (MAE) and root-mean-square error (RMSE) values of 0.22 m and 0.27 respectively are about 4.4% and 5.4% of the spring tide range respectively.

North and east components of velocity at the ADCP location were satisfactorily reproduced by the model, with values of the model skill,  $d_2$ , of about 0.56 and 0.42 respectively (Figure 11, Table 3). The values of the MAE and RMSE being in the range 1 – 3  $\text{cm s}^{-1}$  (Table 3). The scatter plots and histograms shown in Figure 12 and Figure 13 demonstrate that the modelled currents were broadly of the same speed and direction as the observed data.

Table 3. Model performance statistics for sea surface height (SSH), and East and North velocity at the ADCP location from the calibration simulation, November 2018 – February 2019 (ID253).

	SSH	East	North
Skill, $d_2$	0.99	0.56	0.42
Mean Absolute Error (MAE)	0.22 m	0.02 $\text{m s}^{-1}$	0.01 $\text{m s}^{-1}$
Root-Mean-Square Error (RMSE)	0.27 m	0.03 $\text{m s}^{-1}$	0.01 $\text{m s}^{-1}$

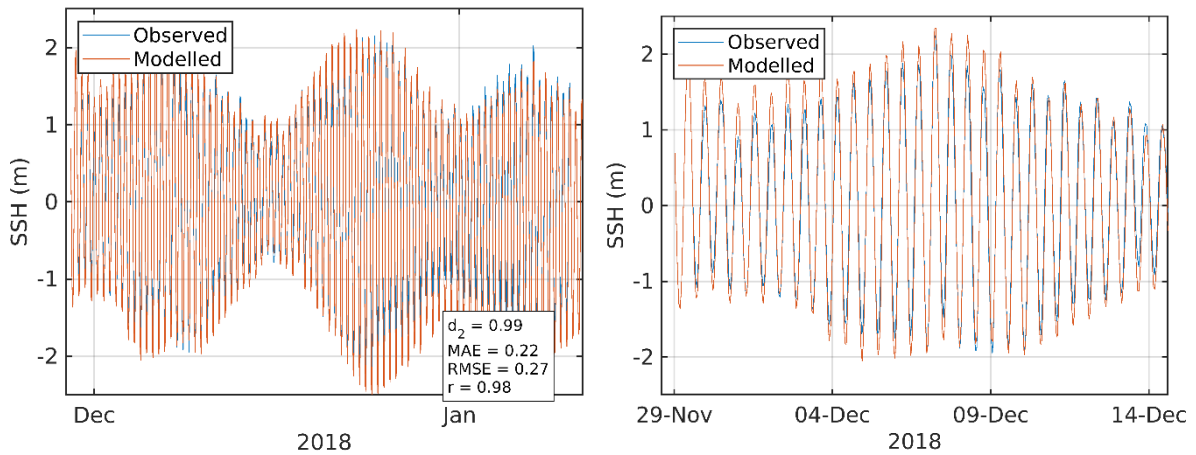


Figure 10. Comparison between observed and modelled sea surface height from November 2018 – February 2019 (ADCP deployment ID253) using model parameter values from Table 1. Both the full record (left) and a subset of 15 days (right) are shown. Observed data are in blue, model results in red.

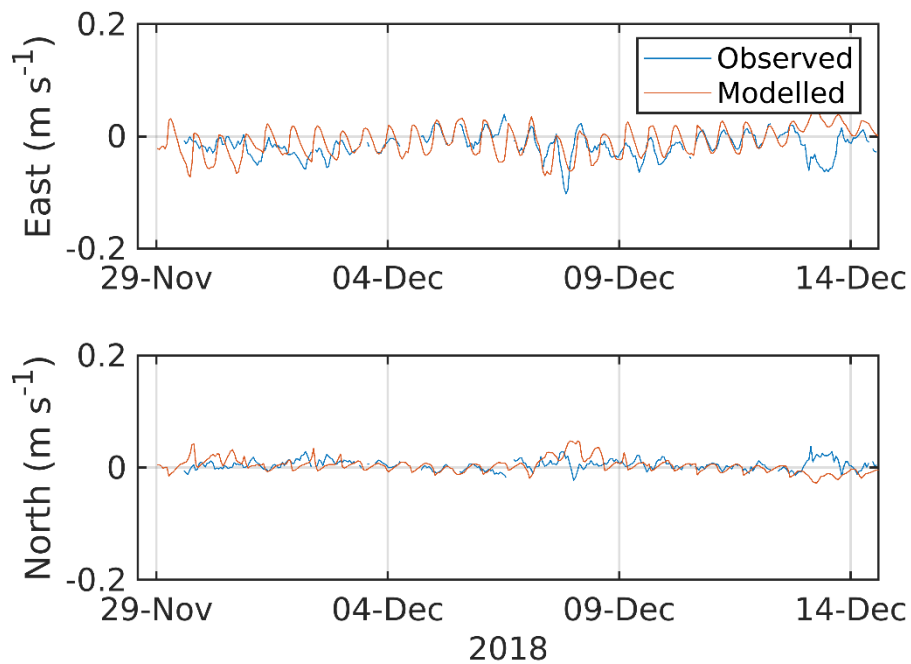


Figure 11. Comparison between observed and modelled East (top) and North (bottom) components of velocity at the ADCP location for 15 days in November 2018 – February 2019 (ID253). Observed data are in blue, model results in red.

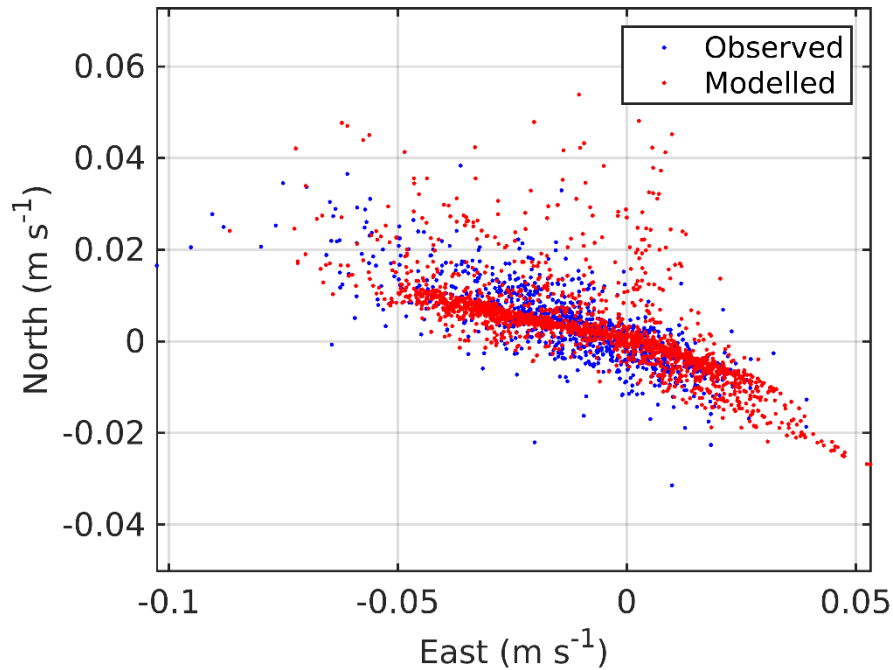


Figure 12. Scatter plot of observed and modelled velocity at the ADCP location from November 2018 – February 2019 (ID253). Observed data are in blue, model results in red.

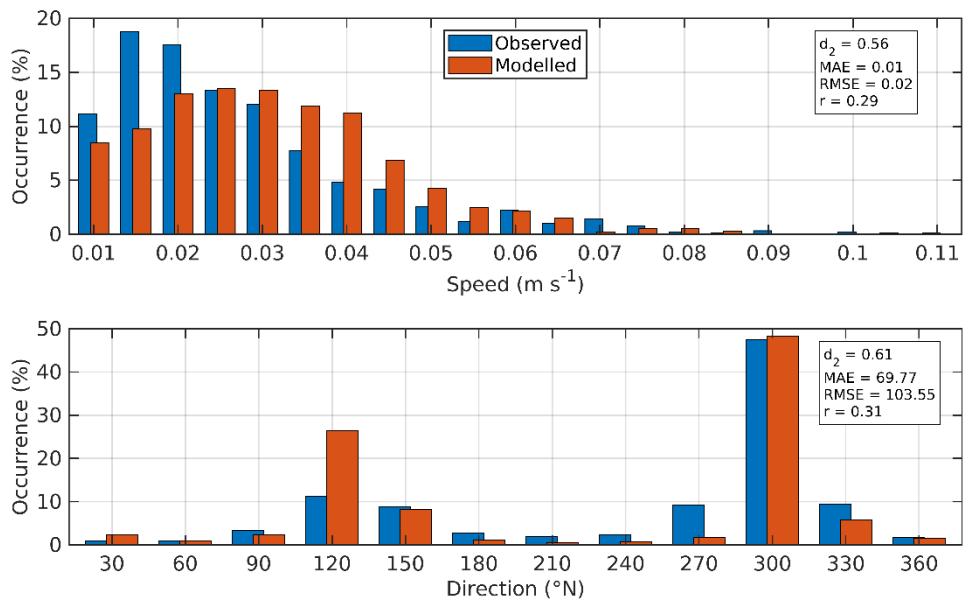


Figure 13. Histograms of observed and modelled current speed (top) and direction (bottom) at the ADCP location from November 2018 – February 2019 (ID253). Observed data are in blue, model results in red.

### 3.3 Validation: November 2018 – February 2019, ID254

At the ADCP location, the sea surface height was reasonably accurately modelled, with model skill of 0.99 (Figure 14, Table 4). The mean absolute error (MAE) and root-mean-square error (RMSE) values of 0.22 m and 0.27 respectively are about 4.4% and 5.4% of the spring tide range respectively.

North and east components of velocity at the ADCP location were satisfactorily reproduced by the model, with values of the model skill,  $d_2$ , of 0.55 for both components of velocity (Figure 15, Table 4). The values of the MAE and RMSE were in the range 2 – 4 cm s<sup>-1</sup> (Table 4). The scatter plots and histograms shown in Figure 16 and Figure 17 demonstrate that the modelled currents were broadly of the same speed and direction as the observed data.

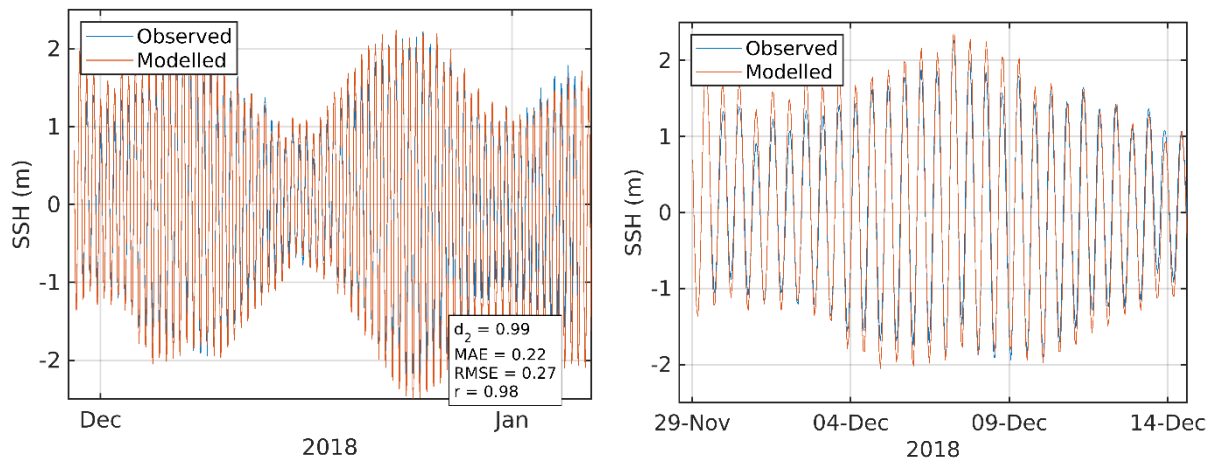


Figure 14. Comparison between observed and modelled sea surface height from November 2018 – February 2019 (ADCP deployment ID254) using model parameter values from Table 1. Both the full record (left) and a subset of 15 days (right) are shown. Observed data are in blue, model results in red.

Table 4. Model performance statistics for sea surface height (SSH), and East and North velocity at the ADCP location from the calibration simulation, November 2018 – February 2019 (ID253).

	SSH	East	North
Skill, $d_2$	0.99	0.55	0.55
Mean Absolute Error (MAE)	0.22 m	0.02 m s <sup>-1</sup>	0.03 m s <sup>-1</sup>
Root-Mean-Square Error (RMSE)	0.27 m	0.03 m s <sup>-1</sup>	0.04 m s <sup>-1</sup>

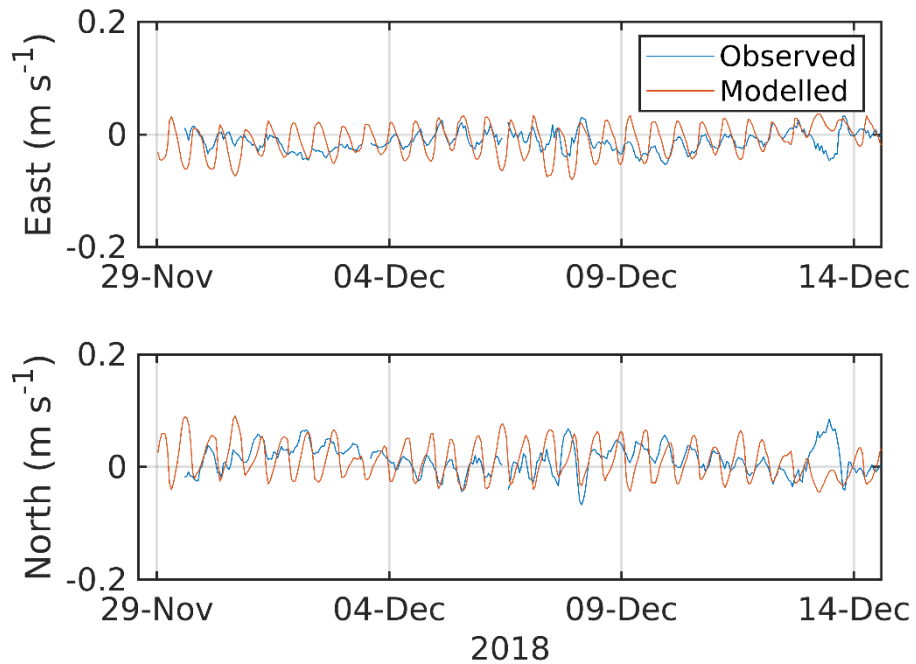


Figure 15. Comparison between observed and modelled East (top) and North (bottom) components of velocity at the ADCP location for 15 days in November 2018 – February 2019 (ID254). Observed data are in blue, model results in red.

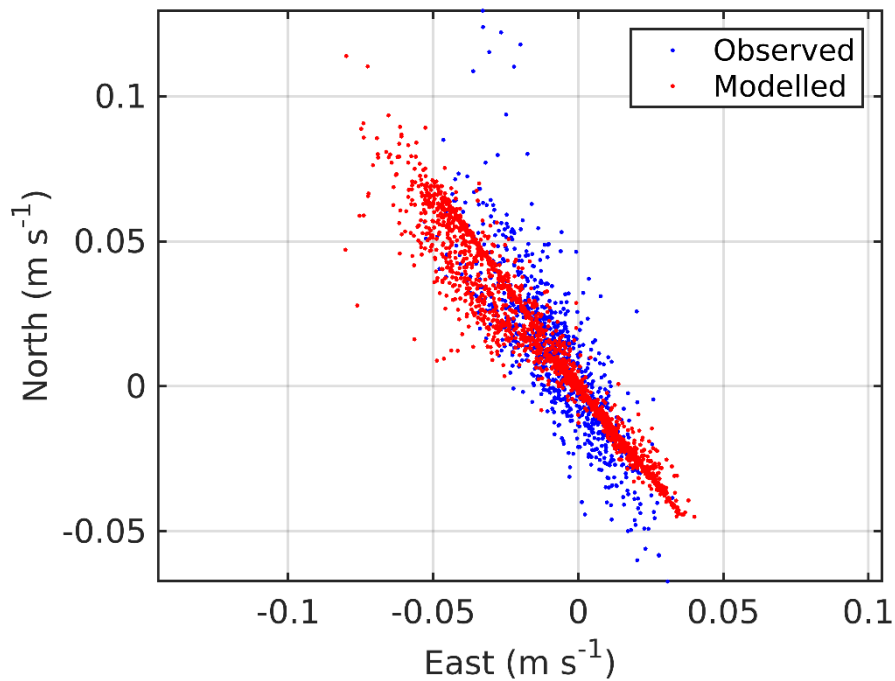


Figure 16. Scatter plot of observed and modelled velocity at the ADCP location from November 2018 – February 2019 (ID254). Observed data are in blue, model results in red.

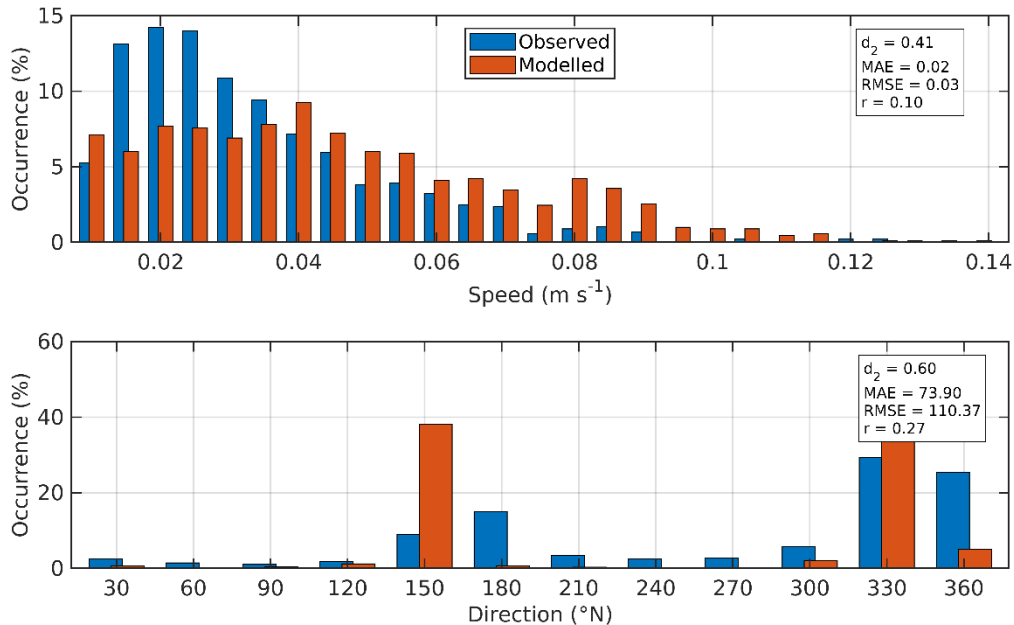


Figure 17. Histograms of observed and modelled current speed (top) and direction (bottom) at the ADCP location from November 2018 – February 2019 (ID254). Observed data are in blue, model results in red.

### 3.4 Validation: April – July 2019, ID275

At the ADCP location, the sea surface height was reasonably accurately modelled, with model skill of 0.99 (Figure 18, Table 5). The mean absolute error (MAE) and root-mean-square error (RMSE) values of 0.21 m and 0.26 respectively are about 4.5% and 5.6% of the spring tide range respectively.

North and east components of velocity at the ADCP location were satisfactorily reproduced by the model, with values of the model skill,  $d_2$ , of about 0.67 and 0.56 respectively (Figure 19, Table 5). The model slightly overpredicted the magnitude of the strongest observed currents (Figure 18 and Figure 19), with values of MAE and RMSE being in the range 1 – 2  $\text{cm s}^{-1}$  (Table 5). The scatter plots and histograms shown in Figure 20 and Figure 21 demonstrate that the modelled currents were broadly of the same speed and direction as the observed data.

Table 5. Model performance statistics for sea surface height (SSH), and East and North velocity at the ADCP location from the calibration simulation, April – July 2019 (ID275).

	SSH	East	North
Skill, $d_2$	0.99	0.67	0.56
Mean Absolute Error (MAE)	0.21 m	0.02 $\text{m s}^{-1}$	0.01 $\text{m s}^{-1}$
Root-Mean-Square Error (RMSE)	0.26 m	0.02 $\text{m s}^{-1}$	0.01 $\text{m s}^{-1}$

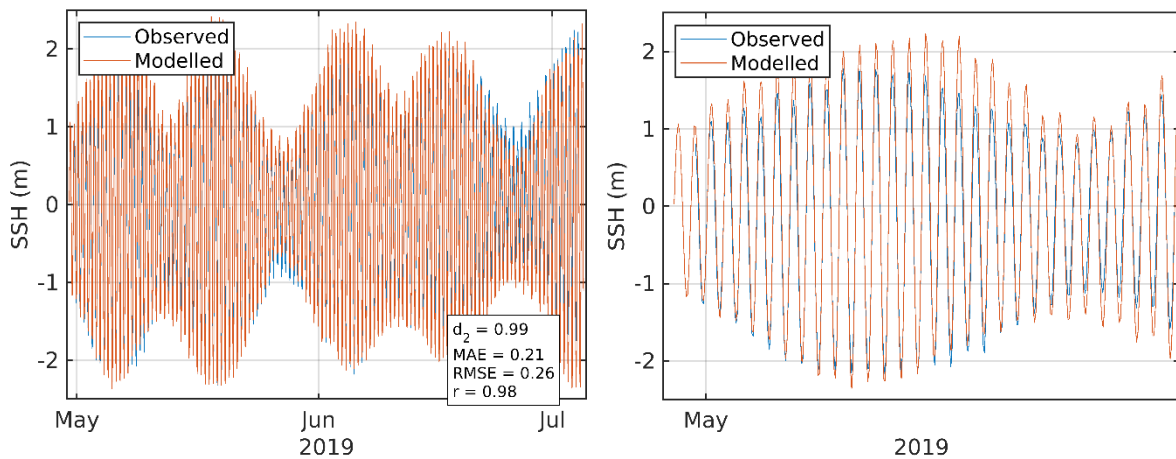


Figure 18. Comparison between observed and modelled sea surface height from April – July 2019 (ID275) using model parameter values from Table 1. Both the full record (left) and a subset of 15 days (right) are shown. Observed data are in blue, model results in red.

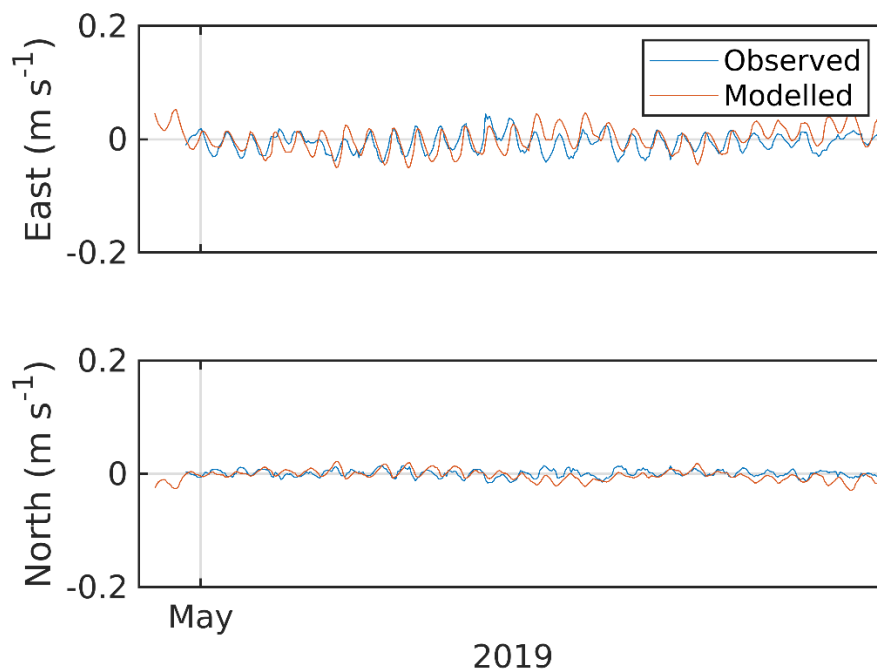


Figure 19. Comparison between observed and modelled East (top) and North (bottom) components of velocity at the ADCP location for 15 days in April – July 2019 (ID275). Observed data are in blue, model results in red.

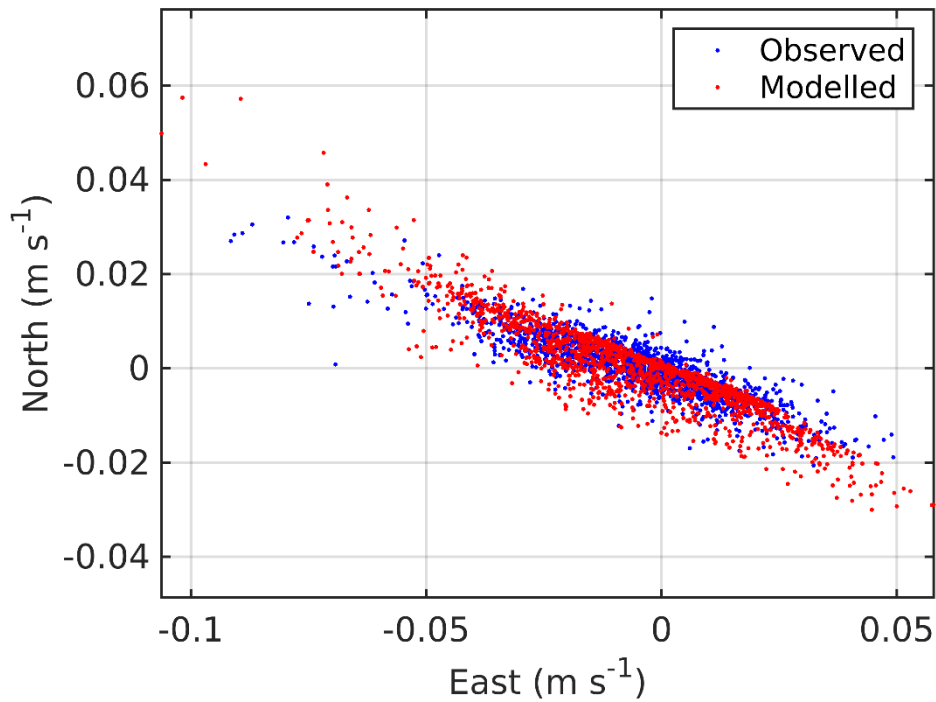


Figure 20. Scatter plot of observed and modelled velocity at the ADCP location from April – July 2019 (ID275). Observed data are in blue, model results in red.

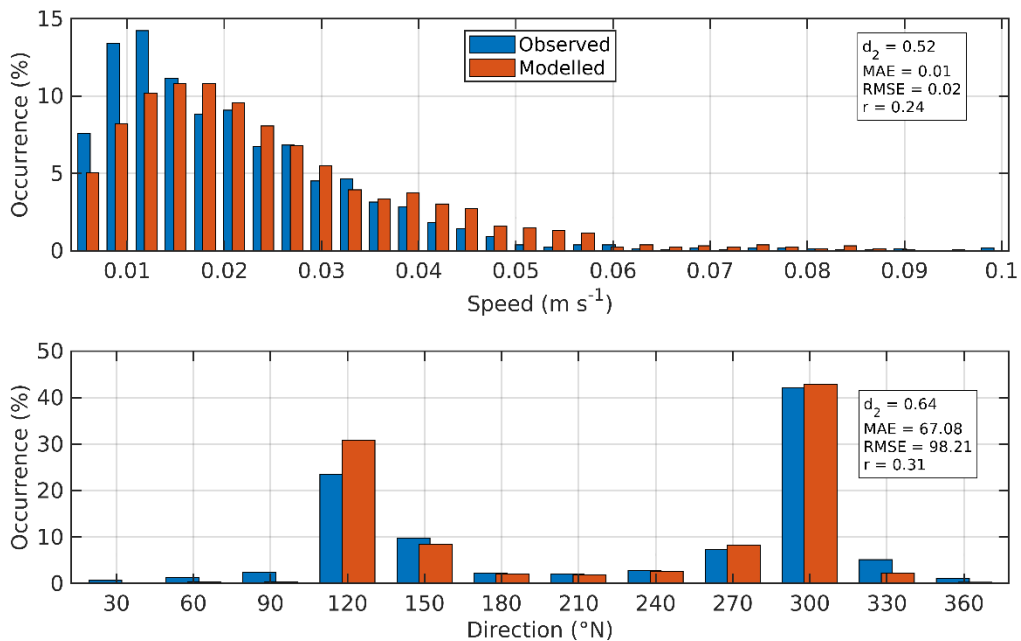


Figure 21. Histograms of observed and modelled speed (top) and direction (bottom) at the ADCP location from April – July 2019 (ID275). Observed data are in blue, model results in red.

#### 4. Modelled Flow Fields

Modelled flood and ebb velocity vectors at spring tides are illustrated in Figure 22. The Loch Hourn site is subject to strong tidal currents flowing in and out of the loch system from the Sound of Sleat. During flood tide, the Craig an t'Sagairt headland generates a cyclonic eddy in the outer loch, and inhibits flow into the loch itself; the incoming flow is instead diverted back toward the Sound of Sleat along the northern shore of the outer loch. On the ebbing tide, a cyclonic eddy is again generated in the outer loch by the southward flowing water in the Sound of Sleat; the outflowing water from central Loch Hourn rounds the Craig an t'Sagairt headland and joins this eddy. The strong eddy in outer Loch Hourn is evident in the mean flow (Figure 23). Mean currents inside the Craig an t'Sagairt headland are weak, including at the farm site. Water leaving the southern shore of central Loch Hourn is directly into the prevailing northward flow in the Sound of Sleat. The dispersion modelling reflected this regime, with the patches of medicine in every modelled case being transported in this way.

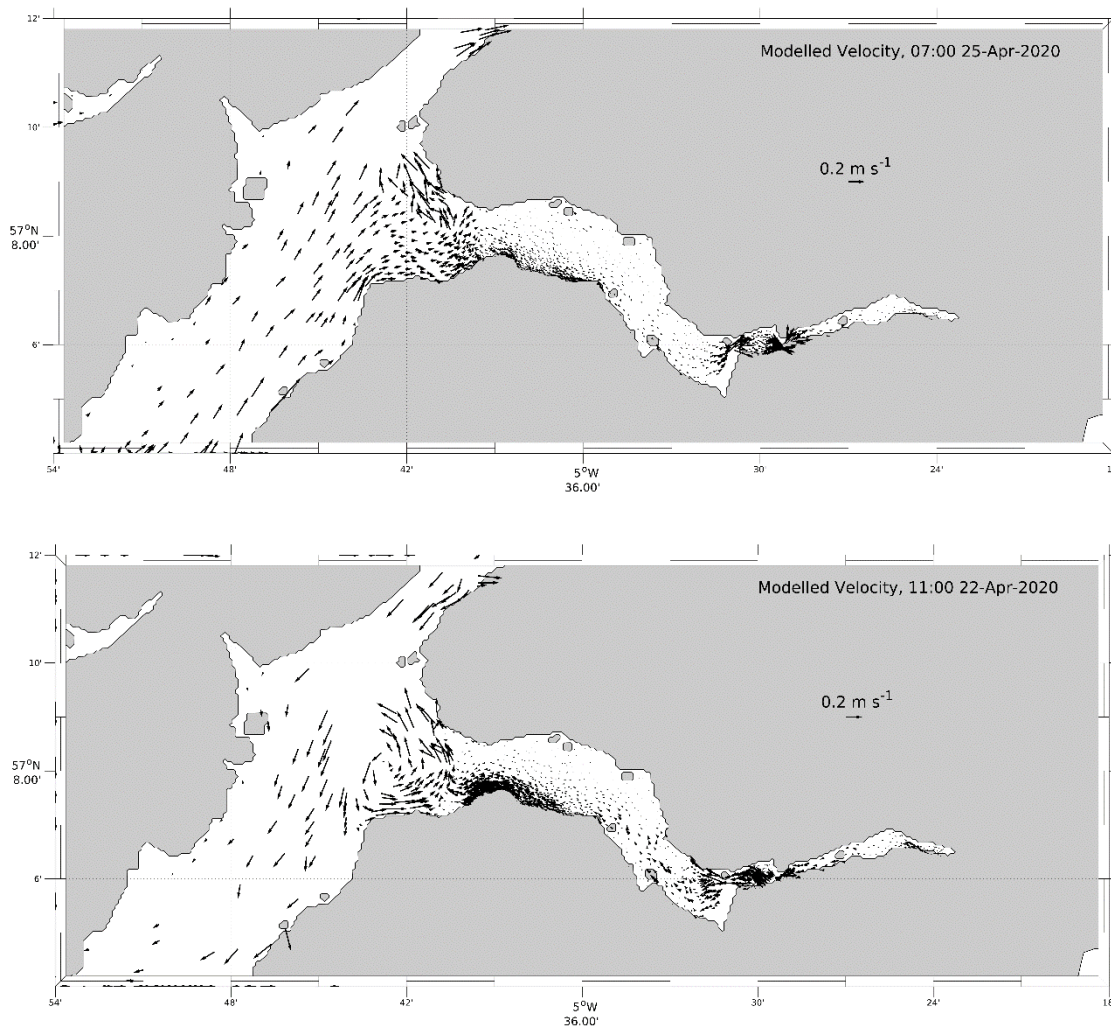


Figure 22. Modelled flood (top) and ebb (bottom) surface current vectors during spring tides on 25<sup>th</sup> April 2020 and 22<sup>nd</sup> April 2020 respectively. For clarity, only 25% of the model vectors are shown, and vectors with a speed greater than 0.3 m s<sup>-1</sup> are also not shown.

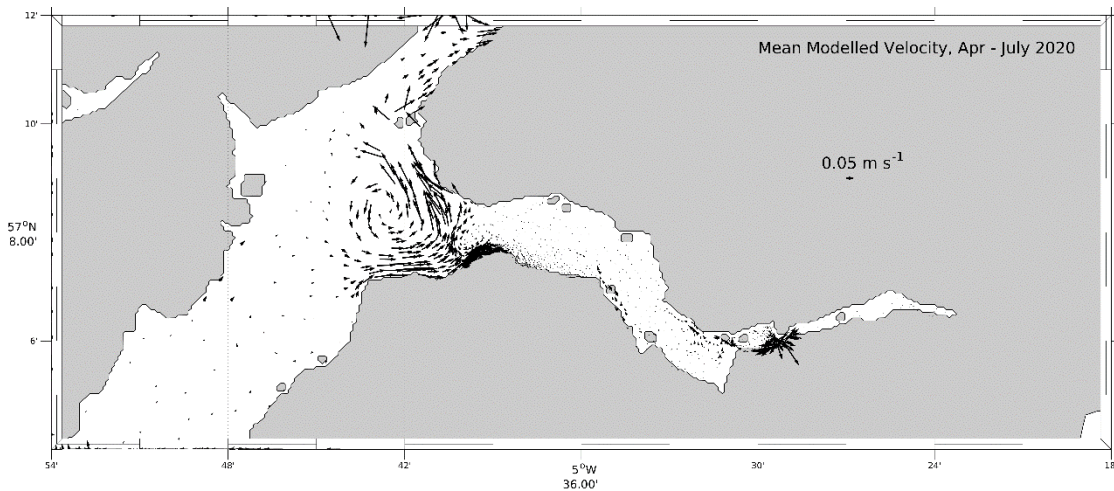


Figure 23. Mean modelled current vectors from 30<sup>th</sup> April – 4<sup>th</sup> July 2020 (ID275). For clarity, only 25% of the model vectors are shown, and vectors with a mean speed greater than 0.2 m s<sup>-1</sup> are also not shown

## 5. References

Casulli, V. 1987. Eulerian-lagrangian methods for hyperbolic and convection dominated parabolic problems. In: Taylor, C., Owen, D., Hinton, E. (Eds.), *Computational Methods for Non-linear Problems*, Pineridge Press, Swansea, U.K., pp. 239–268.

Edwards, A. and Sharples, F., 1986. *Scottish Sea Lochs: A Catalogue*. Scottish Marine Biological Association, Dunstaffnage Marine Laboratory, Oban, U.K., 400pp.

European Centre for Medium-Range Weather Forecasts (ECMWF) 2021, ERA5 Dataset <https://www.ecmwf.int/en/forecasts/datasets/reanalysis-datasets/era5>

Gillibrand, P.A.; Lane, E.M.; Walters, R.A.; Gorman, R.M. 2011. Forecasting extreme sea surface height and coastal inundation from tides, surge and wave setup. *Austr. J. Civil Eng.* 9, 99-112.

Gillibrand, P.A., Walters, R.A., and McIlvenny, J., 2016. Numerical simulations of the effects of a tidal turbine array on near-bed velocity and local bed shear stress. *Energies*, vol 9, no. 10, pp. 852. DOI: 10.3390/en9100852

Lane, E.M.; Gillibrand, P.A.; Arnold, J.R.; Walters, R.A. 2011. Tsunami inundation modeling with RiCOM. *Austr. J. Civil Eng.*, 9, 83-98.

Large, W.G. and Pond, S., 1981. Open ocean momentum flux measurements in moderate to strong winds. *J. Phys. Oceanogr.*, 11, 324—336.

Lewis, M., Neill, S.P., Robins, P., Hashemi, M.R., Ward, S., 2017. Characteristics of the velocity profile at tidal-stream energy sites. *Renewable Energy*, 114, 258-272.

Marine Scotland, 2016. Scottish Shelf Model. Part 4: East Coast of Lewis and Harris Sub-Domain. Available at <https://www.gov.scot/publications/scottish-shelf-model-part-4-east-coast-lewis-harris-sub/pages/4/>

McIlvenny, J. , Tamsett, D., Gillibrand, P.A. and Goddijn-Murphy, L., 2016. Sediment Dynamics in a Tidally Energetic Channel: The Inner Sound, Northern Scotland. *Journal of Marine Science and Engineering*, 4, 31; doi:10.3390/jmse4020031

Plew, D. R.; Stevens, C. L. 2013. Numerical modelling of the effect of turbines on currents in a tidal channel–Tory Channel, New Zealand. *Renew. Energy*, 57, 269-282.

Walters, R. A. 2005a. Coastal ocean models: two useful finite element methods. *Cont. Shelf Res.*, 25(7), 775-793.

Walters, R. A. 2005b. A semi-implicit finite element model for non-hydrostatic (dispersive) surface waves. *Int. J. Num. Meth. Fluids*, 49(7), 721-737.

Walters, R.A. 2016. A coastal ocean model with subgrid approximation. *Ocean Mod.*, 102, 45-54.

Walters, R.A.; Casulli, V., 1998. A robust, finite element model for hydrostatic surface water flows. *Comm. Num. Methods Eng.*, 14, 931–940.

Walters, R.A.; Gillibrand, P.A.; Bell, R.; Lane, E.M. 2010. A Study of Tides and Currents in Cook Strait, New Zealand. *Ocean Dyn.*, 60, 1559-1580.

Walters, R.A., Lane, E.M., Hanert, E. 2009. Useful time-stepping methods for the Coriolis term in a shallow water model. *Ocean Model.*, 28, 66–74. doi: 10.1016/j.ocemod.2008.10.004.

Walters, R.A. ; Lane, E.M.; Henry, R.F. 2008. Semi-lagrangian methods for a finite element coastal ocean model. *Ocean Model.*, 19, 112–124.

Walters, R. A.; Tarbotton, M. R.; Hiles, C. E. 2013. Estimation of tidal power potential. *Renew. Energy*, 51, 255-262.

Willmott, C. J.; Ackleson, S. G.; Davis, R. E.; Feddema, J. J.; Klink, K. M.; Legates, D. R. O'Donnell, J.; Rowe, C. M. 1985. Statistics for evaluation and comparison of models, *J. Geophys. Res.*, 90, 8995– 9005.

Wu, J. 1982. Wind-stress coefficients over sea surface from breeze to hurricane, *J. Geophys. Res.*, 87(C12), 9704–9706, doi:10.1029/JC087iC12p09704.